https://doi.org/10.1016/j.jmps.2022.105121

Revisiting the contact splitting hypothesis: An effective route for enhancing adhesion on rough surface

Hong Hu[1,#], Hongmiao Tian[2,#], Yuan Gao[3], Zhiguo Wan[4], Lei Wang[1], Hailong Xu[1], Chunhui Wang[2], Jinyou Shao[2,*], Zijian Zheng[1,5,6,7,*]

[1]Laboratory for Advanced Interfacial Materials and Devices, School of Fashion and Textiles, The Hong Kong Polytechnic University, Hong Kong SAR, China

[2]State key Laboratory for Manufacturing Systems Engineering, Xi'an Jiaotong University, Xi'an, Shaanxi, 710049, China

[3]Information Science Academy of China Electronics Technology Group Corporation, Beijing 100043, China

[4]School of Mechanical Engineering, Xi'an Shiyou University, Xi'an, Shaanxi, 710049, China

[5]Department of Applied Biology and Chemical Technology, Faculty of Science, The Hong Kong Polytechnic University, Hong Kong SAR, China

[6]Research Institute for Smart Energy (RI-IWEAR), The Hong Kong Polytechnic University, Hong Kong SAR, China

[7]Research Institute for Intelligent Wearable Systems (RISE), The Hong Kong Polytechnic University, Hong Kong SAR, China.

[#]These authors contributed equally to this work

[*]Authors to whom correspondence should be addressed: [Jinyou Shao, jyshao@xjtu.edu.cn; Zijian Zheng, tczzheng@polyu.edu.hk]

ABSTRACT

The contact splitting hypothesis (CSH) has been proposed for around 20 years, which suggests that the patterned or fibrillar surfaces enable very efficient biological attachment systems (e.g., Geckos' seta). However, there is still a debate in academic community on the necessity of the CSH in man-made adhesives, since experiments have indicated that the non-fibrillar surface can also show strong adhesion. This study demonstrates that the surface roughness plays a key role in evaluating the influence of CSH on adhesion by a simple finite element (FE) model. The highly split structures are essentially required for strong adhesion on highly rough surface, but may in turn cause slight adhesion reduction on smooth surface due to the areal loss in the splitting process. With our results, the debate in CSH is explained as an incomplete understanding of an adhesive contact problem, in which the surface roughness is overlooked. Our results further sheds light on the natural selection that climbing animals with heavier body usually evolve finer adhesive structures on their pads., by considering both the surface roughness and its length scale dependence.

Keywords: bio-inspired adhesion, contact splitting hypothesis, fibrillar structures, rough surface, contact model

1. Introduction

Reliable adhesion between objects is of practical importance in industry and our daily life. Traditional pressure sensitive adhesives (PSA) can easily achieve strong

adhesion, but present many drawbacks including difficult removal and surface contamination or damage, because of the chemically synthetic components.[1] With the insight on the remarkable climbing ability of some organisms (e.g., Gecko), the so-called bio-inspired adhesives have been developed in recent decades.[2-4] This new type of adhesive material uses the short-range interaction (e.g., van der Waals force[5]) to produce strong adhesion with good repeatability and environmental friendliness, resulting in various applications from automated pick-and-place operations,[6-9] transfer printing,[10] biomedical devices[11] to climbing or soft robots.[12]

Regardless of the significant progress in the development of bio-inspired adhesive materials, there is still a debate on how to better realize the Gecko-like adhesion for artificial mimics. Some research groups (e.g., Arzt,[13] Carbone,[14] Sitti,[15] Sameoto,[16] Xue,[17] Tian,[18] and Shao[19]) believe that the highly branched fibrillar structures on Geckos' toe pads play a key role in achieving strong adhesion. This idea is based on the contact splitting hypothesis (CSH),[20-23] which was proposed around 20 years earlier and suggested qualitatively that the patterned surfaces with a large number of micro- and nano-scale sub-contacts enabled very efficient attachment mechanisms. This phenomenological hypothesis is widely accepted and leads to the fast development of the field of bio-inspired adhesives, in which the well-designed fibrillar structures are usually adopted. However, some other research groups (e.g., Bartlett and Crosby[1, 24-26]) argue that the fibrillar structures

are likely a natural selection that only endows the organisms with good adhesive functions. It may not be necessary for the man-made adhesives,[24] since experiments have demonstrated that extremely high adhesive force capacity can be obtained by the non-fibrillar adhesives made of soft materials together with the optimized system compliance.[25]

Note that, although both of the above-mentioned two ideals are very successful in guiding the design of the Gecko-like adhesives, they intrinsically contradict each other in considering the mechanism underlying the Gecko's adhesion and its mimics. Observations on the morphology of the toe pads of some other organisms (e.g., Gastrophysa viridula and Carausius morosus[27]) further indicate that the smooth pads (non-fibrillar) can also be as sticky as the hairy pads (fibrillar). In addition, Varenberg et al.,[28] found that there is no statistically significant difference in adhesion between the smooth poly(vinylsiloxane) (PVS) sample and the patterned sample even with more than 10^4 structures per mm^2 sample area. These results lead the researchers to rethink a classic CSH-related issue, i.e., "why are so many adhesive pads hairy?",[29] and to be more careful in understanding the following fundamentals. Does the CSH only validate for partial biological attachment systems? If so, what is the factor determining in which case the CSH can be applied? How strong is the effect of the CSH on adhesion in these cases?

To address these issues, we study the effect of CSH on the adhesion of rough

surfaces by a simple finite element (FE) model. Our results clearly show that the fibrillar surface with highly split structures is essentially required for adhesion on a highly rough surface. However, on the smooth or slightly rough surface, the fibrillar surface in turn presents slightly weaker adhesion than the non-fibrillar surface. Our findings shed light on the long debate in the CSH by revealing two competing effects in the splitting process, i.e., the areal loss and compliance enhancement. In addition, the inverse scaling effect found in many biological attachment systems (i.e., larger body mass, finer adhesive structures), can be also understood by a more general means considering surface roughness as well as its length scale dependence.

2. Model

In our model, a rigid rough surface is in adhesive contact with a deformable part exhibiting a non-fibrillar surface (elastic half space, Fig. 1a) or fibrillar surface with a total structure number N and a lateral length L under the plane strain assumption (Fig. 1b). The area fraction that the structures cover is a constant for fibrillar surface, φ=0.8, while this value for non-fibrillar one could be equal to 1. Note that, in a 2-dimensional problem, the length dimension in the lateral direction can be considered in the unit of area (i.e., L stands for the project area). As roughness can exist over many length scales for most natural or man-made surfaces (e.g., by fracture, wear,[30] or deformation[31]), the rough profile here is described as self-affine fractal with the Hurst exponent H and the root mean square roughness h_{rms}.[32] The interaction is specified by using the 3-9 Lennard-Jones (LJ) traction-separation law, i.e., $\sigma(g) = \frac{8\Delta\gamma}{3\epsilon}\left[\left(\frac{g}{\epsilon}\right)^{-3} - \left(\frac{g}{\epsilon}\right)^{-9}\right]$, where g is the local gap, ϵ is the characteristic length

describing the interaction range, and $\Delta\gamma$ is the interfacial binding energy for an ideal contact pair (perfectly smooth). If the upward direction is set as positive for both the displacement and traction, σ reaches its positive maximum (attractive) value of $\sigma_0 = \frac{16\Delta\gamma}{9\sqrt{3}\epsilon}$ at $g \approx 1.2\epsilon$.[33] The material of the deformable parts is assumed isotropic and linearly elastic and, thus, the reduced modulus of the contact problem is given by $E^* \equiv E/1-\nu^2$, with E the Young's modulus and ν the Poisson ratio. The relative strength of adhesion can be then expressed as a simple length dimension by the ratio of $\Delta\gamma$ to E^*, i.e., $l_a \equiv \Delta\gamma/E^*$.[34, 35] (The modeling and validation processes are described in detail in Appendix A and Appendix B, respectively).

The model is performed in the commercial FE software Abaqus with geometry nonlinearity in consideration. Note also that, the contact problem involving attractive interaction is strongly unstable, particularly for soft material with large interfacial binding energy (large l_a)[36, 37]. The standard Newton-Raphson technique for the implicit integration, which is usually used by other researchers for a static problem,[38, 39] is thus not applicable to a more general model, where l_a may be large.[40] We here used the dynamic/explicit solver instead, and meanwhile strictly constrained the total kinetic energy (E_k) to be around 1% of the strain energy (E_s) by tuning the time period. As such, our model can be considered as a quasi-static process, in which the attraction induced instability is addressed, while the dynamic issue is not important (Appendix C).

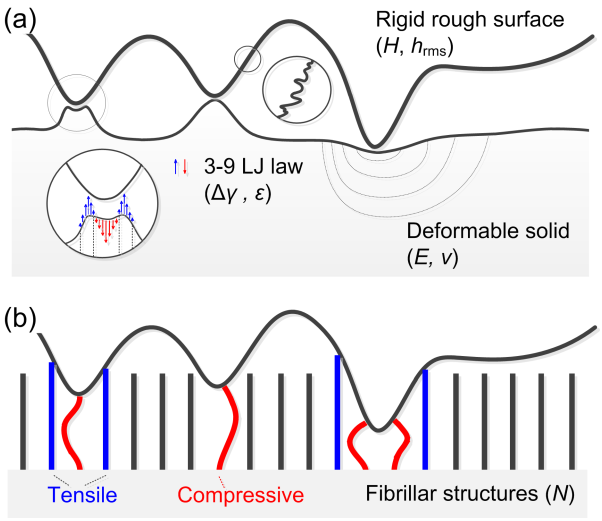

Fig. 1. Schematic of finite element (FE) model where a rigid fractal rough surface is in adhesive contact with a deformable part having a) non-fibrillar surface and b) having many fibrillar structures on the surface, respectively. 3-9 Lennard-Jones (LJ) traction-separation law describes the interaction at the contact interface. With the presence of the surface roughness, the contact is built up partially at the interface. Fibrillar structures may be tensile or compressive as in interaction with the rough surface.

3. Results

3.1 Load behaviors of fibrillar surface

Fig. 2 shows a representative result of the deformation and the corresponding load behaviors as a rigid rough surface ($\tilde{h}_{rms} \equiv h_{rms}/\epsilon$=2, and $\tilde{l}_a \equiv l_a/\epsilon$=0.01) is approached to and retracted from a fibrillar surface (N=256, and $\tilde{L} \equiv L/\epsilon$=320). $\tilde{l}_a$=0.01 is a typical value for some biological attachment systems, e.g., the Gecko's seta made of β-keratin, with $\Delta\gamma$~50 mJ/m^2, E^*~10 GPa and taking ϵ~0.5 nm,[41] while $\tilde{h}_{rms}$=2 indicates a relatively rough profile for $\tilde{L}$=320. The deformations of fibrillar structures were obtained for different dimensionless downward displacements $\tilde{u} \equiv u/\epsilon$=-3.9, -8.0, -9.8, -11.0, and -13, which are labeled as i-v for approaching, and as x-vi for retraction, respectively. The red parts stand for the elements where the upward displacement is greater than the element size Δx, while the displacement of

the blue elements is smaller than Δx or downward. The deformed structures can overlap, because the contacts amongst the structures themselves are neglected. This simplification can significantly enhance the computational efficiency of the model, and only generates limited error on the estimation of the adhesion behavior (Appendix D, and also see [42]).

Structures underneath the valley of the rough surface are first to be stretched by the attractive force (denoted by the rectangle, Fig. 2a) and then compressed with the decrease of $\tilde{u}$. All structures repeat this process, and finally almost buckle as $\tilde{u}$ decreases to $\tilde{u}$=-13. The compliance of these bulked structures can be estimated by calculating the equivalent spring constant (k) of a fiber structure using a simple formula derived by Persson,[43] i.e., $k=4CEI/l^3$, where C is a shape factor with a typical value around 10, I is the moment of inertial, l is the length of the fiber. For the structure in the present study under plane strain condition (a plate actually), the moment of inertial is given by $I=bt^3/12$, where b represents the width of the plate (b=1 in arbitrary length dimension), and t is the thickness. For the structures here, $t/l\approx1/65$, yielding $k/E\approx1.2\times10^{-5}$. With such a small equivalent spring constant, the fibrillar structures behave like a very compliant material. In the retraction process (increase of $\tilde{u}$), structures change from the compressed state to the stretched state, and eventually to the state without any surface traction (Fig. 2b). These structures cannot keep the upright posture, but vibrate instead, as indicated by the dotted circles (also see the animation in the Supplementary Material). This is because the attractive traction

releases suddenly from the structures due to the cutoff LJ function (see Appendix A), which, by the explicit solver, results in the vibration. Note that, the vibration induced kinetic energy has been already included in E_k.

Fig. 2c displays the dimensionless external load $\tilde{\sigma} \equiv F/LE^*$ (F is the external force) as functions of the dimensionless displacement $\tilde{u} \equiv u/\epsilon$. Because of the presence of the surface roughness, the $\tilde{\sigma} - \tilde{u}$ curve is also "rough" with several peak and valley features being observed particularly in the attractive regime ($\tilde{\sigma}$>0). When the overall load becomes repulsive ($\tilde{\sigma}$<0), $\tilde{\sigma}$ slightly changes with $\tilde{u}$, which further indicates the high compliance of the bulked structures (k/E close to 0, also see the animation in Appendix E). Interestingly, the $\tilde{\sigma} - \tilde{u}$ curves in the approaching and retraction processes almost overlap. It implies that the adhesion hysteresis does not exist in our model, which is different from the existing continuum theory.[44, 45] This is because, although the continuum theory predicts the generality of the adhesion hysteresis, the theory itself may not be applicable for the case of highly split fibrillar structures, as suggested by Bettscheider et al.[46] Since the deviation of the load in the approaching and retraction processes may be negligible, the results presented afterwards denote those obtained in the approaching process.

Note that, the $\tilde{\sigma} - \tilde{u}$ curve is an apparent measure of the adhesion behavior, with which the fibrillar layer is actually taken as an interface feature. In addition to the surface roughness and splitting degree, some other geometrical factors, such as, the

height or the density of the fibrillar structures and the thickness of the backing layer,[23, 47-49] can also affect the $\tilde{\sigma}-\tilde{u}$ curve, and thus keep as constants in this study. Two parameters in a $\tilde{\sigma}-\tilde{u}$ curve are usually concerned, i.e., the positive maximum $\tilde{\sigma}$ (pull-off, noted as $\tilde{\sigma}_p$), and the effective interfacial binding energy expressed under our dimensionless system as $\gamma_{eff}=\epsilon E^{*}\widetilde{W}$, where $\widetilde{W}=\int\tilde{\sigma}d\tilde{u}$ is the external work required to break the adhesion, calculated in the interval of $\tilde{u}$ where $\tilde{\sigma}$>0. The width of this interval can also characterize the compliance of the system. To facilitate the description, we define $-\tilde{u}_{+}$ as the dimensionless displacement, at which $\tilde{\sigma}$ changes from attractive to repulsive. In other words, larger $\tilde{u}_{+}$ means a higher compliance.

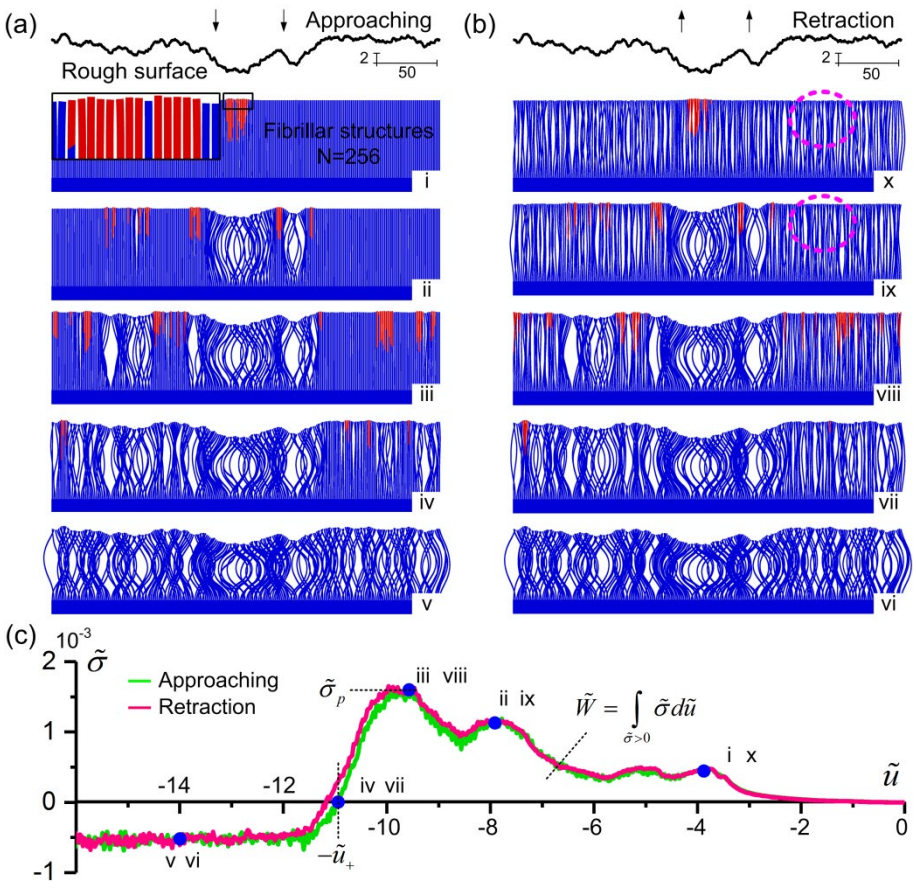

Fig. 2. Representative results of fibrillar structures in adhesive contact with a rough surface by the FE model with H=0.8, $\tilde{h}_{rms}$=2, $\tilde{l}_a$=0.01, $\tilde{L}$=320, and N=256 in the

processes of a) approaching and b) retraction, and c) the corresponding $\tilde{\sigma} - \tilde{u}$ curve. Snapshots showing deformations of fibrillar structures are obtained for $\tilde{u}$= -3.9, -8.0, -9.8, -11.0, and -13, which are labeled as i-v for approaching, and as x-vi for retraction, respectively. In a) and b), the red parts have the upward displacement greater than the mesh size Δx. The structures can overlap because of the neglect of the contacts amongst the structures themselves. The dotted circles indicate the structures with slight vibrations. The deformation in the vertical direction is magnified by two folds. In c), the circular symbols indicate where the corresponding snapshots in a) and b) are obtained. The $\tilde{\sigma} - \tilde{u}$ curves in the approaching and retraction processes almost overlap. $\tilde{\sigma}_p$ is the dimensionless pull-off stress, and $-\tilde{u}_+$ is the dimensionless displacement, at which $\tilde{\sigma}$ changes from attractive to repulsive. $\widetilde{W} = \int_{-\tilde{u}_+}^{0} \tilde{\sigma} d\tilde{u}$ is the dimensionless external work required to break the adhesion.

We then simulated three cases for the non-fibrillar surface, fibrillar surface with *N*=128, and with *N*=256 under the same condition of Fig. 2. To obtain the appropriate statistics, each case was simulated on 10 realizations of randomly rough surfaces. Fig. 3 shows $\tilde{\sigma}$ as functions of $\tilde{u}$. The three cases show a close $\tilde{\sigma}_p$, but significantly different $\tilde{u}_+$. The value of $\tilde{u}_+$ for the non-fibrillar surface is very small ($\tilde{u}_+$=4), but increased to 8.5 for fibrillar surface with *N*=128, and to 11 for *N*=256. The result is in a good agreement with the theory developed by Persson[43] and Jagota et al.[50] In addition, the standard deviation (shadow region) of the curves means that the random process leads to significant variations in the load behaviors even though the statistic parameter of the rough surface is fixed.

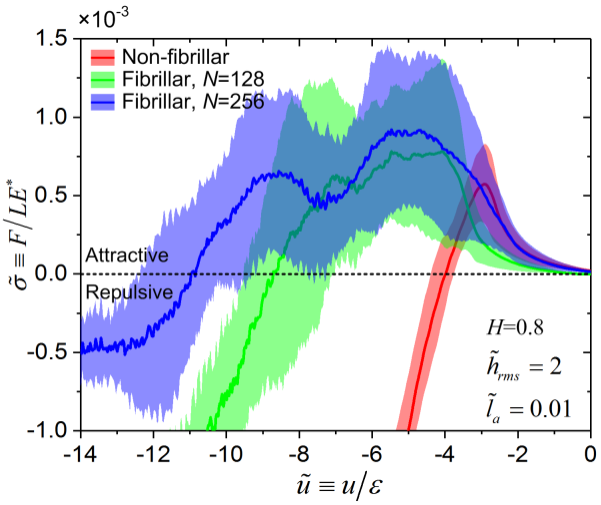

Fig. 3. Dimensionless external load $\tilde{\sigma} \equiv F/LE^*$ as functions of dimensionless displacement $\tilde{u} \equiv u/\epsilon$, for non-fibrillar surface (red), fibrillar surface of N=128 (green), and of N=256 (blue), respectively. Each simulation was performed on 10 realizations of randomly rough surfaces under a fixed condition of H=0.8, $\tilde{h}_{rms}$=2 and $\tilde{L}$=320 with a typical value of $\tilde{l}_a$=0.01. The solid lines and the shadow regions denote the mean and standard deviations of the $\tilde{\sigma} - \tilde{u}$ data of these simulations, respectively.

3.2 Influence of splitting degree on adhesion for different surface roughness

In order to quantitatively understand the CSH in adhesion, more simulations were performed for the non-fibrillar (N=1) or fibrillar surfaces of different N (=2, 8, 32, 64, 128, and 256) and $\tilde{h}_{rms}$ (=0.25, 1 and 5). Because of the large variation in the $\tilde{\sigma} - \tilde{u}$ curve, each simulation was performed for more than 50 times. Figs. 4a-4c compare the effective adhesion by plotting the normalized effective binding energy $\gamma_{eff}/\Delta\gamma \equiv \widetilde{W}/\tilde{l}_a$ as the function of the pull-off stress $\sigma_p/\sigma_0 \equiv \tilde{\sigma}_p/1.03\tilde{l}_a$. The values of these two quantities reach up to their upper bounds of $\gamma_{eff}/\Delta\gamma$=1 and σ_p/σ_0=1 for a perfectly smooth contact pair ($\tilde{h}_{rms}$=0), but quickly decay with increasing the surface roughness.[51] Experiments and theories [52, 53] have demonstrated that adhesion can be in turn enhanced by roughness in the certain case of very large adhesive

strength, e.g., $\tilde{l}_a$≈10 for a rubber material.[54] However, in our model the adhesive strength is much weak ($\tilde{l}_a$=0.01, typical for biological system). The surface roughness induced adhesion enhancement ($\gamma_{eff}/\Delta\gamma$>1 and σ_p/σ_0>1) is thus not observed in the present study. All data are located above the dotted line with the unity slope, which implies a smaller influence of roughness on γ_{eff} than on σ_p.

The mean values of $\gamma_{eff}/\Delta\gamma$ and σ_p/σ_0 are then plotted as functions of the splitting degree, i.e., $\log_2 N$ (Figures 4d-4f). Interestingly, with the increase of *N*, the effective adhesion can either decrease or increase depending on whether the surface is smooth or rough. For the relatively smooth surface (Fig. 4d, $\tilde{h}_{rms}$=0.25), the effective adhesion of both the fibrillar and non-fibrillar surfaces are very close to 1. However, the fibrillar surfaces show slightly weaker adhesion than the non-fibrillar surface (*N*=1) and, furthermore, the effective adhesion of fibrillar surfaces maintains nearly unchanged for different *N*. For the opposite case of large surface roughness (Fig. 4f, $\tilde{h}_{rms}$=5), strong adhesion can be only achieved as *N* reaches up to 256, which is around 6 folds in comparison with the weak adhesion of the non-fibrillar surface and that of the fibrillar one with *N*=2-64. For the surface with intermediate roughness (Fig. 4e, $\tilde{h}_{rms}$=1), the influence of the splitting degree shows a transitional state, in which the adhesion first decreases and then increases as *N* changes from 2 to 256.

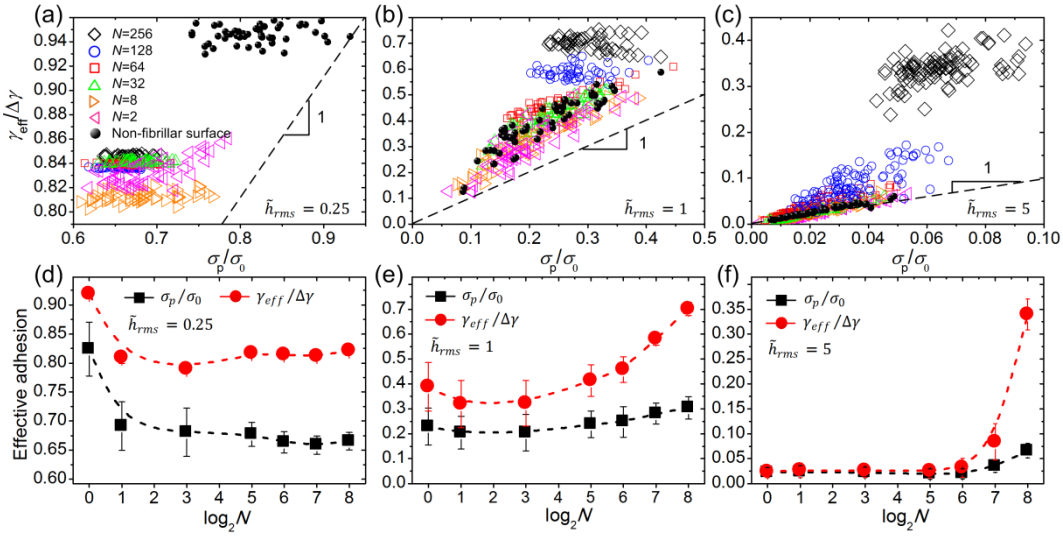

Fig. 4. Influence of splitting degree on effective adhesion ($\gamma_{eff}/\Delta\gamma$ and σ_p/σ_0). $\gamma_{eff}/\Delta\gamma$ was firstly plotted as functions of σ_p/σ_0 for more than 50 realizations of randomly rough surfaces interacting with non-fibrillar surface (N=1) or with fibrillar one (N=2, 8, 32, 64, 128, and 256) for a) $\tilde{h}_{rms}$=0.25, b) $\tilde{h}_{rms}$=1, and c) $\tilde{h}_{rms}$=5, respectively. The dotted lines with unity slope indicate the equal influence of the surface roughness on $\gamma_{eff}/\Delta\gamma$ and σ_p/σ_0. The averaged $\gamma_{eff}/\Delta\gamma$ and σ_p/σ_0 were then plotted as functions of the splitting degree log$_2N$ by the same order of $\tilde{h}_{rms}$ in d) – f). For small $\tilde{h}_{rms}$, adhesion on fibrillar surface is slightly weaker than that on non-fibrillar surface, while for larger $\tilde{h}_{rms}$, strong adhesion can be only achieved for fibrillar surface with high splitting degree.

$\gamma_{eff}/\Delta\gamma$ is then plotted as functions of $\tilde{u}_+$ for different $\tilde{h}_{rms}$, as shown in Fig. 5. The symbol size increases as the splitting degree (log$_2N$) increases from 0-8. For $\tilde{h}_{rms}$=1, and 5, larger N results in both larger $\gamma_{eff}/\Delta\gamma$ and $\tilde{u}_+$. The linear dependence of $\gamma_{eff}/\Delta\gamma$ on $\tilde{u}_+$ indicates a close relation between the strong adhesion and the high compliance. However, this relation cannot be found for $\tilde{h}_{rms}$=0.25, since the data are located at a very narrow range around $\tilde{u}_+ \approx 5$. The arrow indicates the adhesion reduction as the non-fibrillar surface is split to fibrillar one. The effective adhesion for different N is normalized by that for the non-fibrillar surface under the same $\tilde{h}_{rms}$, defined as the adhesion change due to the splitting process, and is plotted as functions of $\tilde{u}_+$ in the inset. The essential role of the

compliance for strong adhesion on the surface with large roughness is easily confirmed. An important suggestion is that, the compliance of a system is often taken as a measure of a load behavior, which is dependent only on material and structure. It should be considered, however, together with the surface roughness in the prediction of adhesion, particularly for the case of fibrillar surface according to our results.

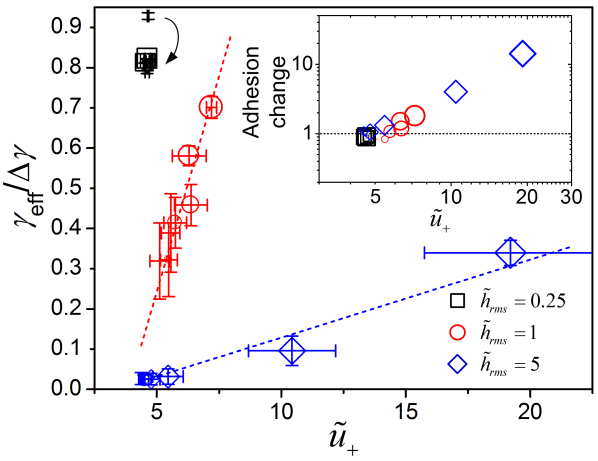

Fig. 5. $\gamma_{eff}/\Delta\gamma$ as functions of $\tilde{u}_+$ for $\tilde{h}_{rms}$=0.25 (square), =1 (sphere), and =5 (diamond), respectively, showing the dependence of adhesion on compliance. The symbol size corresponds to the splitting degree. The role of splitting degree on the adhesion is negligible for $\tilde{h}_{rms}$=0.25, but is important for $\tilde{h}_{rms}$=1, and 5. The arrow indicates the adhesion reduction due to the splitting process. The inset shows that the compliance is of greater importance for adhesion on surface with larger roughness.

3.3 Adhesion on surface with a wide range of roughness

Our results have showed that the splitting process may either weaken (slightly) or strengthen the adhesion, depending on the surface roughness. As such, we believe that there must be a critical rms roughness, $\tilde{h}^c_{rms}$, beyond which the fibrillar surface is stickier, while below which the non-fibrillar one is. We then further studied the adhesion performance of non-fibrillar (N=1) and fibrillar surfaces (N=128, and 256) for a wide range of surface roughness (0.25<$\tilde{h}_{rms}$<25, H=0.8), as shown in Fig. 6. In

these calculations, $\tilde{h}_{rms}$ of the generated rough surfaces with random profiles is logarithmically equally spaced for $\tilde{h}_{rms}$>1, while more calculations are performed for $\tilde{h}_{rms}$<1. The adhesion of fibrillar surface is much stronger than that of non-fibrillar surface when $\tilde{h}_{rms}$>0.6. The adhesion enhancement can even reach to more than one order of magnitude when e.g., $\tilde{h}_{rms}$≈2-10. However, for $\tilde{h}_{rms}$<0.6, $\gamma_{eff}/\Delta\gamma$ of *N*=128 and 256 are smaller than that of non-fibrillar surface (see the inset). The arrow in the inset indicates where the non-fibrillar and fibrillar surfaces are equally sticky, and $\tilde{h}_{rms}^{c}$≈0.6. This value may not be transferable to systems with different geometries and materials, such as, the Hurst exponent of the rough surface, structural height and adhesive strength. Figuring out the quantitative correlation between $\tilde{h}_{rms}^{c}$ and these factors could greatly favor the design of high performance adhesive structures, yet may also require huge computational effort.

For a better understanding of above results, we additionally introduce an analytical model for adhesive contact at rough interface on the basis of the energy equilibrium principle as a benchmark. This model predicts the effective adhesion as a result of two contributions: [55]

$$\frac{\gamma_{eff}}{\Delta\gamma} = \frac{A_{true}}{A_0} - \frac{U_{el}}{\Delta\gamma A_0} \quad (1)$$

where A_{true}/A_0 is the change rate of the surface area upon the contact with A_{true} being the true contact area considering the roughness and A_0 being the project area. $U_{el}/\Delta\gamma A_0$ indicates the ratio of the stored strain energy (U_{el}) density over the project area to $\Delta\gamma$. In many cases, $A_{true}/A_0 \ll 1$, since the contact can be only built up at a

very small fraction of the project area due to the surface roughness. Persson has derived a closed-form expression for Equation (1) in terms of the topographical parameters of the rough surface, given by: [52]

$$\frac{\gamma_{eff}}{\Delta\gamma} = \int_0^{\infty}(1 + x\xi^2)^{\frac{1}{2}}e^{-x}dx - \frac{\pi}{2\tilde{l}_a}\int_{\tilde{q}_0}^{\tilde{q}_1}\tilde{q}^2\tilde{C}(\tilde{q})d\tilde{q} \quad (2)$$

where $\xi = \sqrt{\langle(\nabla h)^2\rangle}$ is the rms gradient or surface slope ($\langle\cdot\rangle$ stands for ensemble averaging), and $\tilde{q} \equiv q\epsilon$, $\tilde{C} \equiv C/\epsilon^4$, denote the dimensionless wave vector, and dimensionless power spectral density (PSD), respectively (more definitions are included in Appendix B).

The dotted blue line in Fig. 6 is the solution of Equation (2) with the same parameters used in the FE model. Note that, Equation (2) is for a 3-dimensional problem, while our FE model is for a 2-dimensional one. To ensure the results comparable, the topographical parameters used in Equation (2) is modified on the basis of a criteria proposed by Scaraggi et al.[56] The analytical solution is in a good agreement with our FE model (non-fibrillar case) for small $\tilde{h}_{rms}$ (dotted line and square symbol overlaps), but it predicts a very weak adhesion for large, e.g., $\tilde{h}_{rms}$~>1, which deviates greatly from our results. This is because Equation (2) is established under the assumption of complete contact, leading $U_{el}/\Delta\gamma A_0$ to increase much more quickly than A_{true}/A_0 with the increase of $\tilde{h}_{rms}$. However, this assumption is released in the FE model.

Equation (1) is a general formula that works for arbitrary process that may cause either of A_{true}/A_0 or $U_{el}/\Delta\gamma A_0$ to change. For the case of a fibrillar surface in

contact with an extremely smooth or a slightly rough surface ($\tilde{h}_{rms} \to 0$), both the elastic energy stored in the deformed structures and the change of the real contact area are small. It means that $U_{el}/\Delta\gamma A_0 \to 0$ and that A_{true} could be approximately equal to the total cross sectional area of the fibers, resulting in $A_{true}/A_0 \approx \varphi$. We may thus obtain $\gamma_{eff}/\Delta\gamma \approx \varphi$ with Equation 1 for the case of $\tilde{h}_{rms} \to 0$. In other words, the analytical solution also predicts the adhesion reduction (φ<1) due to the splitting process for small surface roughness, which is in good agreement with our numerical results (φ=0.8 in the model, $\gamma_{eff}/\Delta\gamma$ is around 0.78-0.80 for $\tilde{h}_{rms}$<0.4). These results reveal the partially areal loss in the splitting process as the reason for the slightly weaker adhesion of fibrillar structures on surface of small roughness. As the split structures can in turn enhance the compliance, which favors the adhesion on highly rough surface, the adhesion behavior of the fibrillar surface is thus a result of these two competing effects, i.e., areal loss and compliance enhancement. The surface roughness is found as a key parameter determining which one could dominate the adhesion.

It is worth noting that the slight reduction in adhesion of fibrillar surface due to the areal loss can be, in principle, minimized by optimizing the geometrical dimensions of the structures. In practice, many effective strategies by modifying the interfacial stress distribution, e.g., using specialized shape as the contact tip,[57-59] or decorating the tip with composite material,[60, 61] have been proposed for further improving the adhesion of the fibrillar structures. These strategies, together with the fact that fibrillar

structures show stronger adhesion on rough surface, strongly support the effectiveness of the CSH (also known as the "smaller is stickier" effect [20]), thus leading to the micro- or nano-patterned surface a promising candidate in a variety of applications.

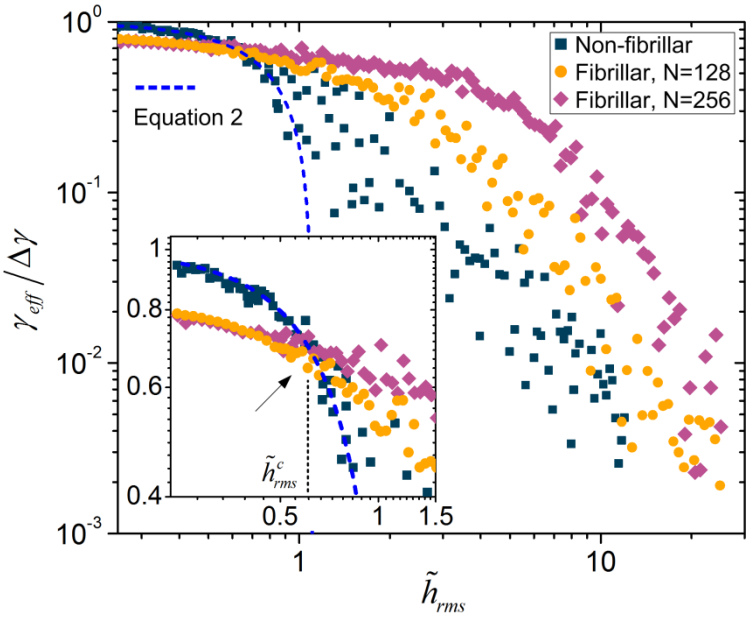

Fig. 6. Adhesion of fibrillar and non-fibrillar surfaces in a wide range of surface roughness $0.25<\tilde{h}_{rms}<25$. The solid symbols indicate the results obtained by the FE model for the non-fibrillar surface (square), fibrillar surface with N=128 (sphere), and with N=256 (diamond), for $\tilde{l}_a$=0.01, $\tilde{L}$=320, and H=0.8. The dotted blue line is the solution of Equation (2). The inset shows more details for the data in $0.25<\tilde{h}_{rms}<1.5$. The critical surface roughness, $\tilde{h}^c_{rms}\approx0.6$, can be found, beyond which the fibrillar surface is stickier, whereas below which the non-fibrillar one is.

4. Discussions

The role of the contact splitting degree in adhesion on slightly or highly rough surfaces has been quantitatively revealed by the FE model, shedding light on the long debate on the CSH. At first sight, the CSH seems to be disadvantageous for adhesion, since the micro- or nano-patterned surface could lose partial project area (gaps amongst split sub-contacts), which can contribute to the local attractive traction. However, this assessment only validates for the surface with small roughness, where the ratio of true contact area to project area dominates the adhesion (i.e., $\gamma_{eff}/\Delta\gamma \approx$

A_{true}/A_0). For a highly rough surface, a higher compliance becomes more important, and the CSH is thus essentially necessary for strong adhesion. In other words, the debate on the CSH may not really conflict with each other, but results from an incomplete understanding of an adhesive contact problem, in which the surface roughness is overlooked in the previous studies. We now return to the experiment performed by Varenberg et al.[28] The patterned surface only involved a simple splitting process in which the strategy for the modification of interfacial stress suggested by Balijepalli et al.[57] was not additionally considered. On account of that the experiment was performed against the smooth substrate, the splitting process was expected to have negligible and even negative impact on enhancing the adhesion.

On the other hand, our results can be also applied to more in-depth understand the functionalities of some biological attachment systems. For example, Arzt et al. [21] have found that animals with larger body mass usually evolve much finer structures on their toe pads (an inverse scaling effect; beetles: m≈10^{-2}-10^{-1} g and N_A≈1, while lizards: m≈10^{1}-10^{2} g and N_A≈10^{3}, where m is the body mass, and N_A is the setae per 100 μm^2). They also proposed a theoretical model using the Johnson-Kendall-Roberts (JKR) theory [62], which quantifies the adhesion enhancement as contacts are split into many sub-contacts. Hui et al.[23] further found that the detachment behavior of the highly split fibrillar interface is easy in the flaw insensitive regime, in which the interface of each structure fails at once and thus an enhanced adhesion is achieved. These studies are widely known as pioneering explorations of the CSH that provides a

clear guideline for the structural design of the bio-inspired adhesives. The contact theories in these models are based on the assumption of smooth surface. However, for the surfaces in real world, the surface roughness can exist on arbitrary length scale.

If the surface roughness is taken into account, the inverse scaling effect of the biological attachment systems can be explained by the following new means. Firstly, Labonte et al.[63] studied across a total number of 225 climbing animal species, and found a relationship between the total pad area and the body mass, i.e., larger body mass leads to larger pad area. Meanwhile, the surface roughness is strongly dependent on the sample area (or sample length) on which the measurement is performed. For a self-affine fractal rough surface, the rms roughness presented on the length scale of λ can be approximately given by a power law of $h_{rms} \sim h_{rms,a}(\lambda/\lambda_a)^H$, where the subscript 'a' indicates the quantity on another length scale.[64] It is very clear that surface appears to be rougher on larger length scale. These two facts easily lead to a simple qualitative conclusion that heavier animals have larger pads, and thus have to face rougher surface. To support the body weight in some certain activities (e.g., climbing), highly split structures with stronger adhesion are essentially required. On the contrary, there is no need for those animals with small body mass as well as small pad area (e.g., beetle) to evolve such complicated attachment system.

5. Conclusions

In conclusion, the contact splitting hypothesis (CSH) was revisited by numerically

modeling the adhesive contact between the fractal rough surface and non-fibrillar or fibrillar surface. Our results clearly show that two competing effects, i.e., areal loss and compliance enhancement, are always associated with, but have different weights in determining the effect of the CSH on adhesion, which is strongly dependent on the surface roughness. On smooth or slightly rough surface, the contact can be built up with generating small amount of strain energy. In this case, the effective adhesion could thus be dominated by the ratio of true contact area to the project area, (i.e., $\frac{\gamma_{eff}}{\Delta\gamma} \approx \frac{A_{true}}{A_0}$, see Equation (1)), leading the fibrillar surface with many gaps (φ<1) to present slightly weaker adhesion in comparison with the non-fibrillar one. However, for the surface with large roughness, the structure compliance becomes more important. The highly split structures with high compliance experience locally larger attractive traction before the overall load becomes repulsive, thus showing much stronger adhesion.

With our results, the long debate in the CSH, i.e., whether the micro- or nano-patterned surface is necessary for the man-made adhesives, can be considered as an incomplete understanding of an adhesive contact problem, in which the surface roughness is overlooked in previous studies. In addition, our results explain why downscaling of the structural dimensions in the biological attachment systems is important for heavier animals in a more general point of view by considering the surface roughness as well as its length scale dependence. Heavier animals usually have larger toe pads, thus have to face rougher surface because of the length scale

dependence of the roughness. Since the highly split fibrillar surface favors the adhesion, these animals evolve finer structures (high split degree) in their toe pads to support their activities. This work gains more in-depth insight into the necessity of the architecture in biological attachment system, and further guides properly the future design of bio-inspired adhesives.

Declaration of Competing Interest

The authors declare that they have no known competing financial interests or personal relationships that could have appeared to influence the work reported in this paper.

Acknowledgements

The authors acknowledge the RGC Senior Research Fellow Scheme (SRFS2122-5S04), the National Natural Science Foundation of China (52175546) and The Hong Kong Polytechnic University (1-ZVQM and 1-CD44).

Appendix A. Finite element modeling

The finite element (FE) model uses many spring-like connector elements (CEs) to simulate the adhesive contact that contains both attractive and repulsive tractions between a rigid and a deformable part having non-fibrillar or fibrillar surface, as shown in Fig. A.1. Each CE links a single control line and a node on the surface of the deformable part. The CEs can only mechanically response to the relative displacement Δu of the two ends in the vertical direction, and generate normal force f_y acting on the

unit length Δx (mesh size) of the deformable part, i.e., $f_{y,i} = \sigma(\Delta u_i)\Delta x$, and $f_{x,i} = 0$. The subscripts "x", "y", and "i" stand for the horizontal direction, vertical direction, and the index of the CE (i=1, 2, …, n; n is the total number of the CEs). Since only the normal force is in consideration, the subscript "y" is omitted afterwards. σ is the traction-separation function, which can have arbitrary form, but here is set as the 3-9 Lennard-Jones (LJ) law, i.e., $\sigma(g) = \frac{8\Delta\gamma}{3\epsilon}\left[\left(\frac{g}{\epsilon}\right)^{-3} - \left(\frac{g}{\epsilon}\right)^{-9}\right]$, where g is the local gap, ε is the characteristic length, and $\Delta\gamma$ is the interfacial binding energy for an ideal condition. The LJ law is generally cutoff for the numerical efficiency as $\sigma(g_1 \le g \le g_2) = \sigma(g)$, $\sigma(g < g_1) = \sigma(g_1)$, and $\sigma(g > g_2) = 0$, where g_1=ε/15, and g_2=15ε in this study.

The lateral project length for the deformable part is L. The bottom side of the deformable part is fixed, and the left- and right-hand sides are periodic boundaries. A downward displacement boundary condition is applied on the control line to make the CEs interact with the deformable part. As CE is always compressed (Δu<0), $\sigma(g)$ should be translated to the left half plane of the axis. The rough contact can be then built up by the further translation transformation of each $\sigma(g)$ function according to the local height profile h_i of the rough surface, which is defined as the relative distance to the minimum of the data set h. Therefore, the normal force f is finally given by: $f_{g,i} = \vartheta_i\sigma(g - g_2 - h_i)\Delta x$, where the subscript "$g$" indicates f as a function of g, ϑ_i is an additional coefficient due to the edge effect. ϑ_i=0.5 as the i-th node is located at the edge of the non-fibrillar surface or fibrillar structures (marked blue), while ϑ_i=1 for the other nodes.

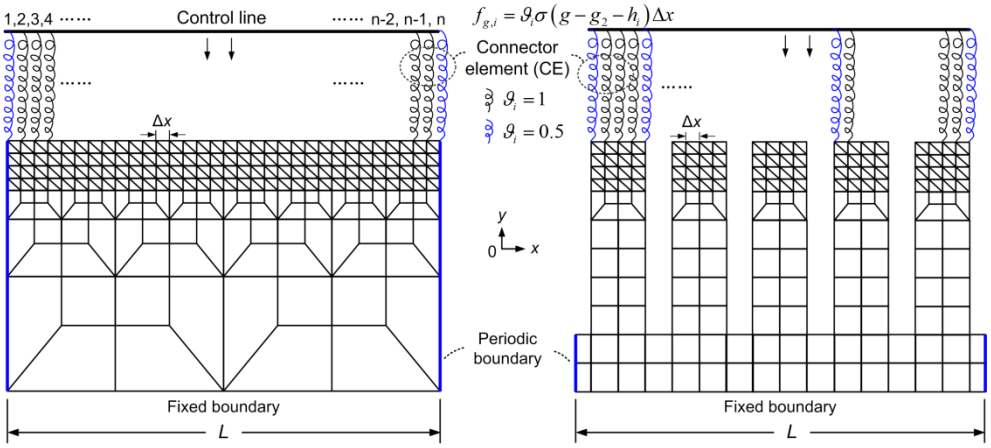

Fig. A.1. Schematic of FE model for rough surface in adhesive contact with a non-fibrillar surface (left) and a fibrillar one (right), respectively. The interaction at the contact interface is implemented by the connector elements (CEs) that link the rigid and deformable parts. The CEs behave like springs, whose constitutive equation is given by $f_{g,i} = \vartheta_i \sigma(g - g_2 - h_i)\Delta x$, where f_g is the normal force acting on per unit length Δx of the deformable part, σ is the 3-9 LJ traction-separation law, g is the range of the interaction cutoff by $g_1 \leq g \leq g_2$, h_i is the local height of the rough profile relative to the minimum of h, h_{min}, the subscript i (=1, 2, 3,…, n; n is the total number of CE) stands for the index of the surface node or CE, and ϑ_i is an additional coefficient depending on whether the i-th node is located at the edge of the non-fibrillar surface or fibrillar structures. Notably, n is different from the number of structure N (see Fig. 1). Since each structure has several nodes, n could be an integral multiple of N. The scale of the schematic does not match with the real model under investigation.

To generate a random sequence of h_i with self-affine fractal characteristic, the Fast Fourier Transformation (FFT) based Monte Carlo approach reported by Wu is used in this study.[65] For a one-dimensional rough counter, the power spectral density (PSD) satisfies $C(q) \sim q^{-2H-1}$ in the interval of $q_0 < q < q_1$, where q is the wave vector and H is the Hurst exponent ($0 < H < 1$), with q_0, q_1, the lower and upper cutoff of q.[66] The project lateral length L and the resolution of the generated rough surface λ_1 determine q_0 and q_1 by $q_0 = 2\pi/L$ and $q_1 = \pi/\lambda_1$, respectively. Fig. A.2a shows the generated rough surfaces $h = h_i$ with different root mean square roughness h_{rms}, under a fixed Hurst

exponent and lateral length, i.e., H=0.8, L/λ_1=1280. Fig. A.2b shows the corresponding PSD, which is obtained with the method proposed by Panda et al.[67]

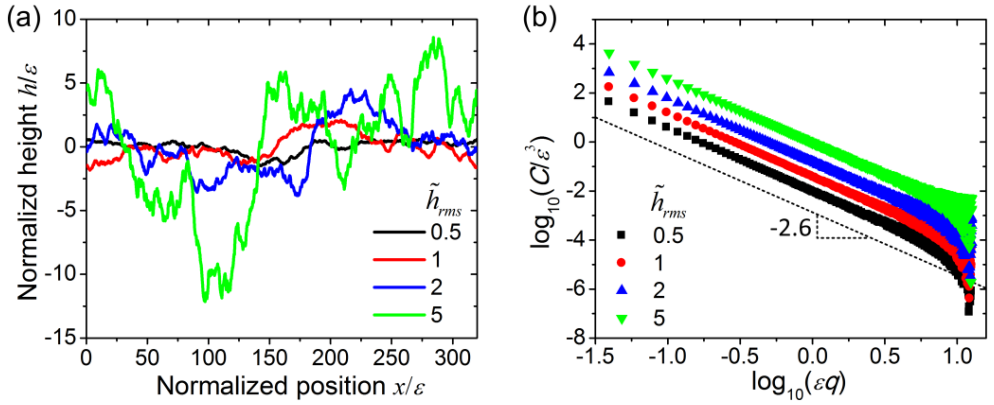

Fig. A.2. Generation of a random sequence of h and the corresponding PSD for different surface roughness of $\tilde{h}_{rms} \equiv h_{rms}/\epsilon$=0.5, 1, 2, and 5, respectively. a) Normalized height h/ε with respect to normalized lateral position x/ε. b) Normalized PSD C/ε^3 as functions of normalized wave vector εq in a double logarithm coordinate plot. The PSD data are almost parallel to the dotted line that has a slope of -2.6, indicating that the random sequence of h (rough profile) is self-affine fractal with Hurst exponent around 0.8 (slope=-2H-1).

Appendix B. Model validation

With the generation of randomly rough surfaces, the calculation can be then performed. Before that, we performed the mesh convergence analysis. It should be pointed out that, the contact in our model is not established via the classic contact algorithm, e.g., establishing a master and a slave surface for a contact pair, but applying the non-uniform and pointwise traction, as a function of local gap, on each node of the element on top of the deformable part. The study on the mesh-size convergence is thus significantly different from the classic FE model. Fig. B.1 shows the methodology for establishing an equivalent model, in which the mesh size changes, while the surface counter does not. If we first set $\Delta x=\lambda_1$ as a pristine model (Fig. B.1a, left), the number of CEs could be equal to that of the random sequence of

h. The traction on each node (solid circles) can be then easily determined. However, if one set $\Delta x > \lambda_1$ (Fig. B.1a, middle, coarse mesh), the traction due to the roughness on the length scale of λ_1 is not applied on the surface. It means that the profile changes (the dotted line), which is not allowed in a mesh convergence analysis. On the other hand, if the mesh is refined to $\Delta x < \lambda_1$ (Fig. B.1b, right, finer mesh), the profile information for the traction on the additional nodes (open circles) that is spaced smaller than λ_1 is by no means known. If one decreases λ_1 by increasing q_1 to seek these profile information in the process of mesh refining, the surface also changes to a new one, making the study also not a mesh convergence analysis.

Therefore, only refining the mesh with $\lambda_1/\Delta x > 1$ is allowed, and the tractions on the additional nodes need to be artificially defined. According to the Saint Venant's principle, which is usually used in FE analysis to determine the nodal traction, the traction distribution can be in arbitrary form as long as the total traction in a very narrow region does not change.[68] In the present model, we use the simplest load distribution, i.e., the nodal traction in an pristine model is scattered equally to the refined nodes over two adjacent regions, both of which is half of λ_1. Fig. B.1b illustrates an example of this methodology. Assume that three tractions, $f_{g,i-1}$, $f_{g,i}$, and $f_{g,i+1}$, are loaded on three nodes (solid circle), correspondingly. The concerned node is labeled as "o". The middle points between any two neighboring nodes are marked with "×". Two middle points that are most close to node "o" are labeled as "I" and "II", respectively. If the mesh is refined by η folds, the traction on the refined nodes between, but not including, the middle points "I" and "II" is $f_{g,i}/\eta$. On the node at the

middle point, the traction could be, for example, point "I", $(f_{g,i-1}/\eta+f_{g,i}/\eta)/2$. All the nodal tractions can be calculated by this methodology.

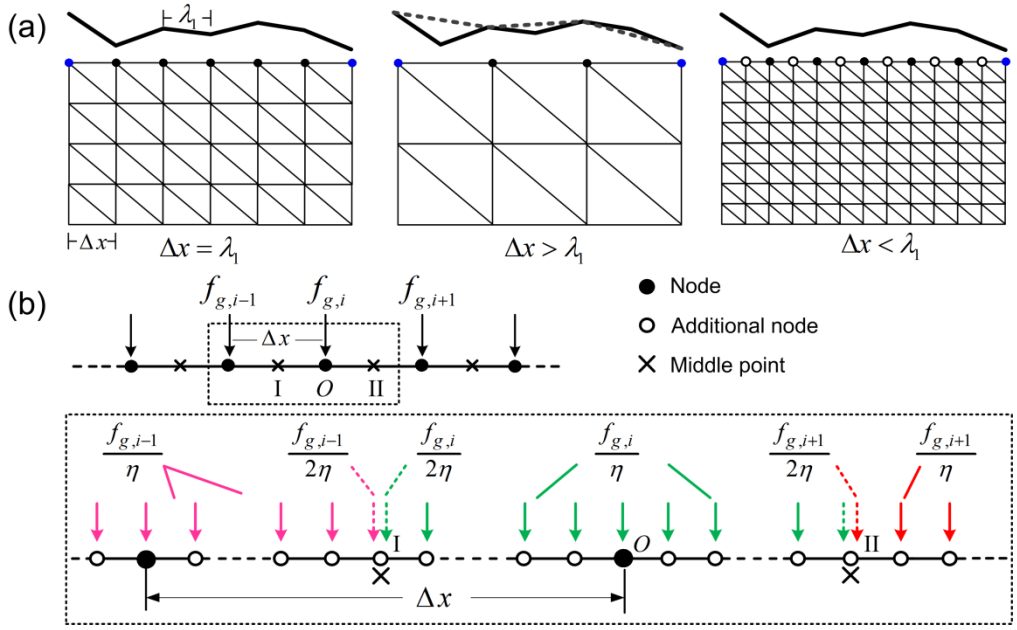

Fig. B.1. Methodology for mesh refinement in FE model. a) Schematic showing a pristine mesh (left, $\lambda_1/\Delta x=1$), a coarser mesh (middle, $\lambda_1/\Delta x<1$), and a finer mesh (right, $\lambda_1/\Delta x>1$), respectively. If the coarser mesh is adopted, the local traction due to the rough profile on the length scale smaller than Δx cannot be applied correctly on the surface. The rough surface actually changes to a new one (the dotted line). Therefore, we only perform the calculation for the finer mesh, i.e., $\lambda_1/\Delta x>1$. b) An example of the simplest loading methodology. The nodal traction within the region coded by the dotted rectangle is shown in details.

To validate the FE model, the results between the non-fibrillar surface and rough surface by a numerical calculation (Green's function molecular dynamics, GFMD) reported by Persson and Scaraggi were introduced as a benchmark.[69] The parameters in our model were taken from Figures 15 and 18 of Ref.[69], i.e., H=0.8, E^*=1.33×10^3 GPa, q_0=2.5×10^5 m^{-1}, q_1=64q_0, and h_{rms}=0.52 nm. Note that, the results in Ref. [69] are for a 3-dimensional problem. To ensure the results comparable, the

surface roughness used in our model (a 2-dimensional model) is modified on the basis of a criteria proposed by Scaraggi et al.[56]

Fig. B.2a shows the load behaviors ($\sigma - u$ curve) for $\lambda_1/\Delta x$=1, 2, 4, and 8, with $\Delta\gamma$=0.1 and 0.2 J/m^2, respectively. There is no significant difference as the mesh-size decreases. Since the pristine model can lead to the results very close to the highly refined one, we will use this mesh size, i.e., $\lambda_1/\Delta x$=1, in the following calculations for fibrillar surfaces. On the other hand, the pull-off stress data σ_p of these models are additionally compared with the GFMD results (Fig. B.2b). The good agreement between them indicates the effectiveness of our FE model in predicting the adhesion on rough surface.

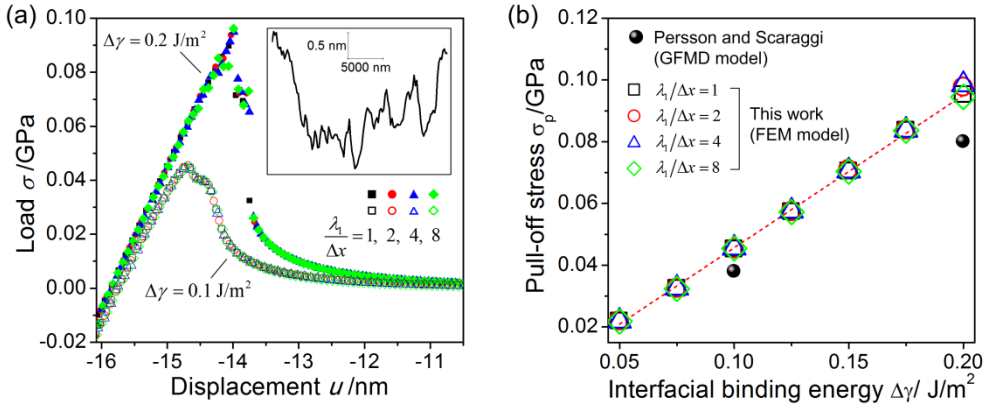

Fig. B.2. Mesh convergence analysis. a) External load σ as functions of displacement u for different mesh sizes of $\lambda_1/\Delta x$=1, 2, 4, and 8 with $\Delta\gamma$=0.1 and 0.2 J/m^2. The inset shows the rough surface used in these calculations. b) Pull-off stress σ_p as functions of interfacial binding energy $\Delta\gamma$, which was predicted by the GFMD method of Persson and Scaraggi (solid symbols), and our FE model (open symbols), for different mesh sizes, respectively. The parameters in these calculations were taken from Figures 15 and 18 of Ref.[69], i.e., H=0.8, E^*=1.33×10^3 GPa, q_0=2.5×10^5 m^{-1}, q_1=64q_0, and h_{rms}=0.52 nm. The dimensional quantities can facilitate the comparison with the results shown in Ref.[69].

Appendix C. A quasi-static model by minimizing the kinetic energy

To guarantee our model a quasi-static process even using a dynamic/explicit solver,

the total kinetic energy E_k should be strictly constrained. Fig. C.1 compares E_k and the total strain energy E_s as functions of the external load in both the approaching and retraction processes. E_s is nearly two orders of magnitude lager than E_k, implying the insignificance of the dynamic issue in our model. Note that, at the very beginning of the approaching process, i.e., $\tilde{\sigma} \to 0$, E_k and E_s are close to each other. However, this cannot affect significantly our estimation of the adhesion, since it only takes place for a very narrow range of $\tilde{\sigma}$.

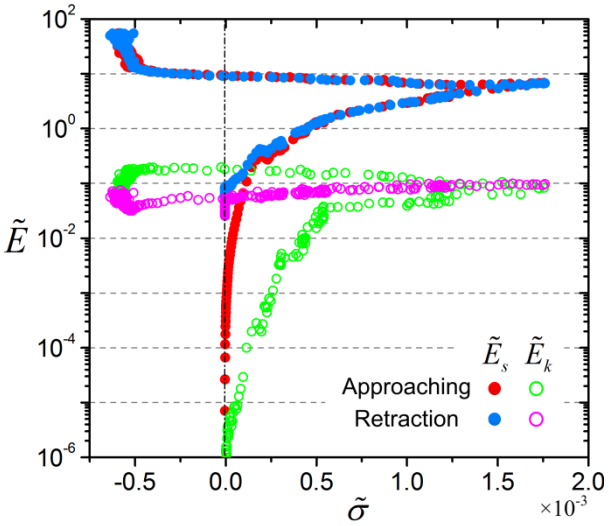

Fig. C.1. Comparison in energy as a rough surface is approaching to and retracted from a fibrillar surface. The parameters in this calculation are as the same as that in Fig. 2, but the surface profile may be different due to the random process. The dimensionless kinetic energy $\tilde{E}_k \equiv E_k/\Delta\gamma\epsilon^2$ (open symbols), and dimensionless strain engery $\tilde{E}_s \equiv E_s/\Delta\gamma\epsilon^2$ (solid symbols) are plotted as functions of dimensionless external load $\tilde{\sigma}$.

Appendix D. Comparison between results with or without self-contact among structures

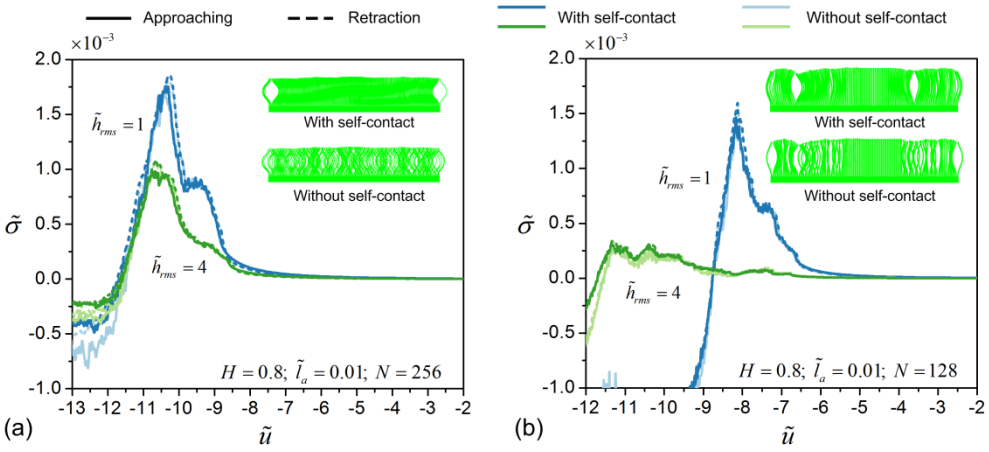

Fig. D. 1. Comparison of load behaviors with or without self-contact among fibrillar structures for different splitting degrees and surface roughness. a) $\tilde{\sigma}-\tilde{u}$ curves for N=256, $\tilde{h}_{rms}$=1 and =4. b) $\tilde{\sigma}-\tilde{u}$ curves for N=128, $\tilde{h}_{rms}$=1 and =4. Other parameters are as the same as those in Fig. 2 (H=0.8, $\tilde{l}_a$=0.01). The solid and dotted lines stand for the results in approaching and retraction stage, respectively, while the darker and lighter lines stand for those with and without self-contact in the model, respectively. The darker and lighter lines can nearly overlap particularly for $\tilde{\sigma}$>0 (attractive traction), indicating that neglecting the self-contact among structures affects insignificantly the estimation of the adhesion behavior. To improve the computational efficiency, all the calculations in this study were performed under the approximation without any self-contact. The insets display the deformation of the structures when the downward displacement $\tilde{u}$ reaches the maximum. The inset in a) corresponds to N=256, and $\tilde{h}_{rms}$=1, while that in b) corresponds to N=128, and $\tilde{h}_{rms}$=4. The deformation in vertical direction is magnified by two folds.

Appendix E. Supplementary material

The following is the supplementary material related to this study.

Video S1. Upper panel: Deformations of fibrillar structures as a rough surface is approached to and retracted from them. The parameters used in this calculation is as the same as those in Fig. 1. Because of the random process, the rough surface may present different profiles. In the retraction process, the structures can vibrate because of the explicit/dynamics solver in our model. However, our model can be considered a quasi-static process in which the dynamic issue is not important (see below). Lower-left plane: The dimensionless external load $\tilde{\sigma} \equiv F/LE^*$ as a function of the

dimensionless displacement of the rough surface $\tilde{u} \equiv u/\epsilon$. As $\tilde{\sigma}$ changes from attractive to repulsive, $\tilde{\sigma}$ appears to slightly change with the decrease of $\tilde{u}$. This is because the equivalent spring constant of the buckled structures are very small. Lower-right plane: Comparison of the dimensionless kinetic energy $\tilde{E}_k \equiv E_k/\Delta\gamma\epsilon^2$ and strain energy $\tilde{E}_s \equiv E_s/\Delta\gamma\epsilon^2$ as functions of $\tilde{\sigma}$. $\tilde{E}_s$ is nearly two orders of magnitude lager than $\tilde{E}_k$, implying the insignificance of the dynamic issue in our model.

Reference

[1] M. D. Bartlett and A. J. Crosby, High Capacity, Easy Release Adhesives From Renewable Materials, *Adv. Mater.* **26**, 3405 (2014).

[2] E. Arzt, H. Quan, R. M. McMeeking, and R. Hensel, Functional surface microstructures inspired by nature – From adhesion and wetting principles to sustainable new devices, *Prog. Mater. Sci.* **120**, 100823 (2021).

[3] W. Wang, Y. Liu, and Z. Xie, Gecko-Like Dry Adhesive Surfaces and Their Applications: A Review, *J. Bionic Eng.* **18**, 1011 (2021).

[4] J. A. Booth and R. Hensel, Perspective on statistical effects in the adhesion of micropatterned surfaces, *Appl. Phys. Lett.* **119**, 230502 (2021).

[5] K. Autumn, Y. A. Liang, S. T. Hsieh, W. Zesch, W. P. Chan, T. W. Kenny, R. Fearing, and R. J. Full, Adhesive force of a single gecko foot-hair, *Nature* **405**, 681 (2000).

[6] X. Li, X. Li, L. Li, T. Sun, Y. Meng, and Y. Tian, Trumpet-shaped controllable adhesive structure for manipulation of millimeter-sized objects, *Smart Mater. Struct.* **30**, 115003 (2021).

[7] Y. Wang, X. Zhang, R. Hensel, and E. Arzt, Sliding Mechanism for Release of Superlight Objects from Micropatterned Adhesives, *Adv. Mater. Interfaces* **9**, 2101764 (2022).

[8] H. Hu, D. Wang, H. Tian, Q. Huang, C. Wang, X. Chen, Y. Gao, X. Li, X. Chen, Z. Zheng, and J. Shao, Bioinspired Hierarchical Structures for Contact-Sensible Adhesives, *Adv. Funct. Mater.* **32**, 2109076 (2022).

[9] J. Zhao, X. Li, Y. Tan, X. Liu, T. Lu, and M. Shi, Smart Adhesives via Magnetic Actuation, *Adv. Mater.* **34**, 2107748 (2022).

[10] S. Zhang, H. Luo, S. Wang, Z. Chen, S. Nie, C. Liu, and J. Song, A thermal actuated switchable dry adhesive with high reversibility for transfer printing, *Int. J. Extrem. Manuf.* **3**, 035103 (2021).

[11] T. Kim, J. Park, J. Sohn, D. Cho, and S. Jeon, Bioinspired, Highly Stretchable, and Conductive Dry Adhesives Based on 1D–2D Hybrid Carbon Nanocomposites for All-in-One ECG Electrodes, *ACS Nano* **10**, 4770 (2016).

[12] M. Spenko, Making Contact: A Review of Robotic Attachment Mechanisms for Extraterrestrial Applications, *Adv. Intell. Syst.* **n/a**, 2100063 (2022).

[13] M. Samri, J. Thiemecke, E. Prinz, T. Dahmen, R. Hensel, and E. Arzt, Predicting the adhesion strength of micropatterned surfaces using supervised machine learning, *Mater. Today* **53**, 41 (2022).

[14] G. Carbone and E. Pierro, Sticky Bio-inspired Micropillars: Finding the Best Shape, *Small* **8**, 1449 (2012).

[15] S. Kim and M. Sitti, Biologically inspired polymer microfibers with spatulate tips as repeatable fibrillar adhesives, *Appl. Phys. Lett.* **89**, 261911 (2006).

[16] D. Sameoto and C. Menon, A low-cost, high-yield fabrication method for producing optimized biomimetic dry adhesives, *J. Micromech. Microeng.* **19**, 115002 (2009).

[17] Q. Liu, D. Tan, F. Meng, B. Yang, Z. Shi, X. Wang, Q. Li, C. Nie, S. Liu, and L. Xue, Adhesion Enhancement of Micropillar Array by Combining the Adhesive Design from Gecko and Tree Frog, *Small* **17**, 2005493 (2021).

[18] X. Li, P. Bai, X. Li, L. Li, Y. Li, H. Lu, L. Ma, Y. Meng, and Y. Tian, Robust scalable reversible strong adhesion by gecko-inspired composite design, *Friction* **10**, 1192 (2022).

[19] J. Shao, X. Chen, X. Li, H. Tian, C. Wang, and B. Lu, Nanoimprint lithography for the manufacturing of flexible electronics, *Sci. China Technol. Sci.* **62**, 175 (2019).

[20] M. Kamperman, E. Kroner, A. del Campo, R. M. McMeeking, and E. Arzt, Functional Adhesive Surfaces with “Gecko” Effect: The Concept of Contact Splitting, *Adv. Eng. Mater.* **12**, 335 (2010).

[21] E. Arzt, S. Gorb, and R. Spolenak, From micro to nano contacts in biological attachment devices, *Proc. Natl. Acad. Sci. U. S. A.* **100**, 10603 (2003).

[22] H. Gao, X. Wang, H. Yao, S. Gorb, and E. Arzt, Mechanics of hierarchical adhesion structures of geckos, *Mech. Mater.* **37**, 275 (2005).

[23] C.-Y. Hui, N. J. Glassmaker, T. Tang, and A. Jagota, Design of biomimetic fibrillar interfaces: 2. Mechanics of enhanced adhesion, *J. R. Soc. Interface* **1**, 35 (2004).

[24] M. D. Bartlett, A. B. Croll, D. R. King, B. M. Paret, D. J. Irschick, and A. J. Crosby, Looking Beyond Fibrillar Features to Scale Gecko-Like Adhesion, *Adv. Mater.* **24**, 1078 (2012).

[25] D. R. King, M. D. Bartlett, C. A. Gilman, D. J. Irschick, and A. J. Crosby, Creating Gecko-Like Adhesives for "Real World" Surfaces, *Adv. Mater.* **26**, 4345 (2014).

[26] M. D. Bartlett, A. B. Croll, and A. J. Crosby, Designing Bio-Inspired Adhesives for Shear Loading: From Simple Structures to Complex Patterns, *Adv. Funct. Mater.* **22**, 4985 (2012).

[27] J. M. R. Bullock, P. Drechsler, and W. Federle, Comparison of smooth and hairy attachment pads in insects: friction,adhesion and mechanisms for direction-dependence, *J. Exp. Biol.* **211**, 3333 (2008).

[28] M. Varenberg, B. Murarash, Y. Kligerman, and S. N. Gorb, Geometry-controlled adhesion: revisiting the contact splitting hypothesis, *Appl. Phys. A* **103**, 933 (2011).

[29] W. Federle, Why are so many adhesive pads hairy?, *J. Exp. Biol.* **209**, 2611 (2006).

[30] B. N. J. Persson, Adhesion between Elastic Bodies with Randomly Rough Surfaces, *Phys. Rev. Lett.* **89**, 245502 (2002).

[31] A. R. Hinkle, W. G. Nöhring, R. Leute, T. Junge, and L. Pastewka, The emergence of small-scale self-affine surface roughness from deformation, *Sci. Adv.* **6**, eaax0847 (2020).

[32] L. Pastewka and M. O. Robbins, Contact area of rough spheres: Large scale simulations and simple scaling laws, *Appl. Phys. Lett.* **108**, 221601 (2016).

[33] J. Joe, M. D. Thouless, and J. R. Barber, Effect of roughness on the adhesive tractions between contacting bodies, *J. Mech. Phys. Solids* **118**, 365 (2018).

[34] L. Pastewka and M. O. Robbins, Contact between rough surfaces and a criterion for macroscopic adhesion, *Proc. Natl. Acad. Sci. U. S. A.* **111**, 3298 (2014).

[35] G. Violano, L. Afferrante, A. Papangelo, and M. Ciavarella, On stickiness of multiscale randomly rough surfaces, *J. Adhes.* **97**, 509 (2021).

[36] N. Jia, Y. Yao, Z. Peng, and S. Chen, Surface effect in nanoscale adhesive contact, *J. Adhes.* **97**, 380 (2021).

[37] R. A. Sauer and S. Li, An atomic interaction-based continuum model for adhesive contact mechanics, *Finite Elem. Anal. Des.* **43**, 384 (2007).

[38] Z. Song and K. Komvopoulos, Adhesion-induced instabilities in elastic and elastic–plastic contacts

during single and repetitive normal loading, *J. Mech. Phys. Solids* **59**, 884 (2011).

[39] F. Jin, Q. Tang, X. Guo, and H. Gao, A generalized Maugis-Dugdale solution for adhesion of power-law graded elastic materials, *J. Mech. Phys. Solids* **154**, 104509 (2021).

[40] H. Radhakrishnan and S. D. Mesarovic, Adhesive contact of elastic spheres revisited: numerical models and scaling, *Proceedings of the Royal Society A: Mathematical, Physical and Engineering Sciences* **465**, 2231 (2009).

[41] T. W. Kim and B. Bhushan, Adhesion analysis of multi-level hierarchical attachment system contacting with a rough surface, *J. Adhes. Sci. Technol.* **21**, 1 (2007).

[42] T. Li, Z. Y. Huang, Z. C. Xi, S. P. Lacour, S. Wagner, and Z. Suo, Delocalizing strain in a thin metal film on a polymer substrate, *Mech. Mater.* **37**, 261 (2005).

[43] B. N. J. Persson, On the mechanism of adhesion in biological systems, *J. Chem. Phys.* **118**, 7614 (2003).

[44] A. Sanner and L. Pastewka, Crack-front model for adhesion of soft elastic spheres with chemical heterogeneity, *J. Mech. Phys. Solids* **160**, 104781 (2022).

[45] F. Jin, W. Zhang, Q. Wan, and X. Guo, Adhesive contact of a power-law graded elastic half-space with a randomly rough rigid surface, *Int. J. Solids Stuct.* **81**, 244 (2016).

[46] S. Bettscheider, D. Yu, K. L. Foster, R. M. McMeeking, E. Arzt, R. Hensel, and J. A. Booth, Breakdown of continuum models for spherical probe adhesion tests on micropatterned surfaces, *J. Mech. Phys. Solids* **150**, 104365 (2021).

[47] N. J. Glassmaker, A. Jagota, C.-Y. Hui, and J. Kim, Design of biomimetic fibrillar interfaces: 1. Making contact, *J. R. Soc. Interface* **1**, 23 (2004).

[48] S. Chen and A. K. Soh, Tuning the geometrical parameters of biomimetic fibrillar structures to enhance adhesion, *J. R. Soc. Interface* **5**, 373 (2008).

[49] R. Long, C.-Y. Hui, S. Kim, and M. Sitti, Modeling the soft backing layer thickness effect on adhesion of elastic microfiber arrays, *J. Appl. Phys.* **104**, 044301 (2008).

[50] A. Jagota and S. J. Bennison, Mechanics of Adhesion Through a Fibrillar Microstructure1, *Integr. Comp. Biol.* **42**, 1140 (2002).

[51] H. Hu, S. Zhao, W. Wang, Y. Zhang, Y. Fu, and Z. Zheng, Prediction of adhesion between randomly rough surfaces by order statistics, *Appl. Phys. Lett.* **119**, 071603 (2021).

[52] B. N. J. Persson, Adhesion between an elastic body and a randomly rough hard surface, *Eur. Phys.*

J. E **8**, 385 (2002).

[53] G. Palasantzas and J. T. M. De Hosson, Influence of surface roughness on the adhesion of elastic films, *Phys. Rev. E* **67**, 021604 (2003).

[54] P. R. Guduru, Detachment of a rigid solid from an elastic wavy surface: Theory, *J. Mech. Phys. Solids* **55**, 445 (2007).

[55] B. N. J. Persson and E. Tosatti, The effect of surface roughness on the adhesion of elastic solids, *J. Chem. Phys.* **115**, 5597 (2001).

[56] M. Scaraggi, C. Putignano, and G. Carbone, Elastic contact of rough surfaces: A simple criterion to make 2D isotropic roughness equivalent to 1D one, *Wear* **297**, 811 (2013).

[57] R. G. Balijepalli, M. R. Begley, N. A. Fleck, R. M. McMeeking, and E. Arzt, Numerical simulation of the edge stress singularity and the adhesion strength for compliant mushroom fibrils adhered to rigid substrates, *Int. J. Solids Stuct.* **85-86**, 160 (2016).

[58] X. Zhang, Y. Wang, R. Hensel, and E. Arzt, A Design Strategy for Mushroom-Shaped Microfibrils With Optimized Dry Adhesion: Experiments and Finite Element Analyses, *J. Appl. Mech.* **88**, 031015 (2020).

[59] J. Zhao, T. Lu, T. Pan, X. Li, and M. Shi, Mushroom-Shaped Micropillar With a Maximum Pull-Off Force, *J. Appl. Mech.* **89**, 071009 (2022).

[60] R. G. Balijepalli, S. C. L. Fischer, R. Hensel, R. M. McMeeking, and E. Arzt, Numerical study of adhesion enhancement by composite fibrils with soft tip layers, *J. Mech. Phys. Solids* **99**, 357 (2017).

[61] S. C. L. Fischer, E. Arzt, and R. Hensel, Composite Pillars with a Tunable Interface for Adhesion to Rough Substrates, *ACS Appl. Mater. Interfaces* **9**, 1036 (2017).

[62] K. L. Johnson, K. Kendall, A. D. Roberts, and D. Tabor, Surface energy and the contact of elastic solids, *Proceedings of the Royal Society of London. A. Mathematical and Physical Sciences* **324**, 301 (1971).

[63] D. Labonte, C. J. Clemente, A. Dittrich, C.-Y. Kuo, A. J. Crosby, D. J. Irschick, and W. Federle, Extreme positive allometry of animal adhesive pads and the size limits of adhesion-based climbing, *Proc. Natl. Acad. Sci. U. S. A.* **113**, 1297 (2016).

[64] S. You and M. P. Wan, Mathematical Models for the van der Waals Force and Capillary Force between a Rough Particle and Surface, *Langmuir* **29**, 9104 (2013).

[65] J.-J. Wu, Simulation of rough surfaces with FFT, *Tribol. Int.* **33**, 47 (2000).

[66] Q. Li, M. Popov, A. Dimaki, A. E. Filippov, S. Kürschner, and V. L. Popov, Friction Between a Viscoelastic Body and a Rigid Surface with Random Self-Affine Roughness, *Phys. Rev. Lett.* **111**, 034301 (2013).

[67] S. Panda, A. Panzade, M. Sarangi, and S. K. Roy Chowdhury, Spectral Approach on Multiscale Roughness Characterization of Nominally Rough Surfaces, *J. Tribol.* **139**, 031402 (2016).

[68] B. Karp and D. Durban, Saint-Venant's Principle in Dynamics of Structures, *Appl. Mech. Rev.* **64**, 020801 (2011).

[69] B. N. J. Persson and M. Scaraggi, Theory of adhesion: Role of surface roughness, *J. Chem. Phys.* **141**, 124701 (2014).